Focal-Plane Array Receiver Systems
for Space Communications

M. Britcliffe,[1] D. Hoppe,[1] and V. Vilnrotter[2]

Typical ground antennas intended for use in space communications require large apertures operating at high frequencies. The challenge involved with these applications is achieving the required antenna performance in terms of antenna aperture efficiency and pointing accuracy. The utilization of a focal-plane array in place of a standard single-mode feed minimizes these problems. This article discusses the key elements required to implement a focal-plane array on a large high-frequency antenna. The example of the NASA Deep Space Network 70-m antennas operating at 32 GHz has been chosen to illustrate these advantages. The design of a suitable feed and low-noise cryogenically cooled amplifier and the required signal-processing techniques are described. It is shown that adaptive least mean-square algorithms can be applied to the output of the array elements, in order to obtain the optimum combining weights in real time, even in the presence of dynamic interference (nearby spacecraft in the array's field of view or planetary radiation). This adaptive optimization capability maximizes the combined output signal-to-noise ratio in real time, ensuring maximum data throughput in the communications link when operating in the presence of receiver noise and external interference generally present during planetary encounters.

I. Introduction

This article discusses the conceptual design and the expected performance of a cryogenically cooled focal-plane array (FPA) receiver system for space communications applications. Focal-plane-array-based receivers are investigated as a solution for recovering lost focal-plane energy in large antennas for 32-GHz deep-space communication [1]. Researchers in large-aperture radio astronomy have also used array feeds to produce multiple beams on the sky in the 26- to 30-GHz band [2].

Array-based receivers have the potential to provide the lowest cost and highest performance of any approach to implementing high-frequency operation on large antennas. A properly designed array receiver has the potential to solve virtually all problems associated with this application. These problems include large-scale reflector surface accuracy error from gravity deformation, subreflector positioning error, and

---

static- and wind-induced antenna pointing error. In addition, the array enables a single antenna to receive downlink signals from several different directions simultaneously.

To date, microwave array receivers for large antennas intended for communication have largely been based on arrays of closely spaced horns coupled to low-noise amplifier (LNA) systems. Studies of the focal-plane distribution of the Deep Space Network (DSN) 70-m antennas has shown that closely spaced horns do not result in adequate coupling of the energy in the focal plane into the feed for many pointing/distortion scenarios [3].

The system described here uses a focal-plane array of patch antennas that is designed to allow the energy in the focal plane to be more efficiently coupled into the receiver. In addition to the increase in coupling efficiency, the patch antenna approach allows the LNAs to be coupled directly to the elements. This lowers the complexity of the system and fabrication cost. It also results in a more compact array that reduces the size of the receiver package. This reduces the required cryogenic cooling and makes implementation in a limited space environment easier.

Although the array receiver configuration presented here is applicable to virtually any antenna, the modeling and electromagnetic design is based on 32-GHz (Ka-band) operation on a DSN 70-m antenna. The 70-m antenna was chosen as an example for several reasons. First of all, Ka-band operation on a 70-m antenna operation is a worst-case scenario. The ratio of the operating wavelength to antenna diameter (λ/diameter $= 1.4 \times 10^{-4}$) is challenging and would normally require adaptive compensation of the main reflector surface or similar costly complicated techniques. Secondly, a 32-GHz array receiver using horn antennas was demonstrated on a 70-m antenna [1], and the available data allow a direct comparison to show the advantage of the patch array antenna configuration. Finally, there is a substantial amount of data available on the actual surface deformation of the 70-m antenna for analysis and modeling [4].

This article addresses the key technical challenges to implementing the technology. It begins with a description of the overall system hardware. This is followed by a theoretical calculation of the focal-plane array performance. This is followed by a discussion of the signal processing system required to take the raw array output and accomplish optimum combining in a realistic environment including noise and interference. Next a design for a cryogenic system to support the integrated focal-plane array feed/LNA is presented along with an estimate of the expected cryogenic and noise performance.

II. System Description

The system consists of a cryogenically cooled path array antenna connected to monolithic microwave integrated circuit (MMIC) LNAs. The largest array considered here is a square 9×9 array with 81 elements. The LNA outputs are routed out of the cryogenic cooler to a phase-locked radio frequency (RF)-to-baseband converter. The complex in-phase and quadrature (IQ) signals from the converter are then routed to the signal processor. The signal processor combines the array output into a single data stream. The data can be upconverted to a suitable intermediate frequency (IF) to be processed by an existing receiver such as the DSN Block V receiver. The signal processor also computes any pointing offset from the array data and sends that information to the antenna pointing system. A simplified block diagram for a single-element chain is shown in Fig. 1.

III. Theoretical Calculation of FPA Performance

In this section, we will discuss the electromagnetic modeling of the focal-plane array. We have chosen to use the DSN 70-m dual-shaped antenna for the performance investigation. The main reason for choosing this particular antenna is that it suffers from significant gain loss as a function of elevation angle. The gain loss is a result of distortion of the primary reflector, which changes as the antenna tips in elevation, causing a relative change between the orientation of the gravity vector and the primary reflector. This
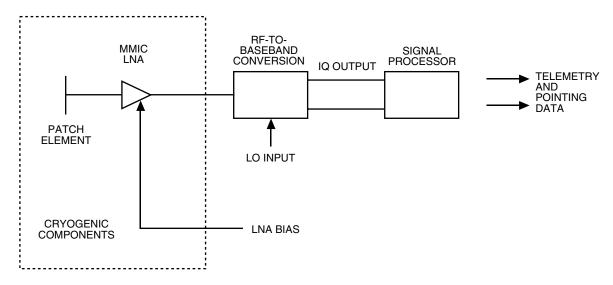
Fig. 1. System block diagram.

phenomenon also exists, to a lesser extent, on the DSN 34-m antennas as well. As we shall see, the focal-plane array is quite effective in compensating for this particular gain loss. In addition, we wish to illustrate the ability of the focal-plane array to reduce blind-pointing requirements for the antenna. Finally, we describe the signal-processing system required to take the raw array output and accomplish optimum combining in a realistic environment including noise and interference.

A. Physical Optics Model

Figure 2 illustrates the geometry for the study. A plane wave is incident on the shaped primary reflector, which also includes an elevation-angle-dependent distortion. The collected energy then travels to the shaped secondary reflector, where it is focused at a point slightly above the primary reflector. At this point, the energy would normally be collected by a corrugated feed horn. For this study, we allow the energy to pass through this primary focus to a magnifying ellipse that re-images the primary focus onto a secondary focal plane. The focal-plane array resides at this secondary focus. As we shall see, this re-imaging allows us to adjust the focal-plane spot size to better match the element size used in the focal-plane array.

For the present study, a simple patch array model was used [5]. The patches are each approximately 0.49 wavelengths square and are assumed to reside on an air dielectric. The element spacing was chosen to be approximately 0.7 wavelengths. This particular spacing was found to nearly equalize the capture area of the patch with the physical area of an array cell while minimizing mutual coupling effects. If instead the patch array were realized using a non-air dielectric, the scale of the structure would be reduced proportionately. This scaling can be compensated for by adjusting the magnification value of the system, and thus no generality is lost by assuming an air dielectric.

The response of the antenna is computed on an element-by-element basis. Physical optics is used to compute the far-field pattern of the antenna for excitation of each of the individual array elements. This calculation is repeated for each of the antenna elevation angles and for each of the magnification values investigated. Reciprocity is used to compute the excitation of each of the elements when a plane wave from a given direction is incident on the antenna. In all cases, careful accounting for all of the incident energy must be maintained, including mutual coupling between the array elements. All calculations were carried out at 32.05 GHz.
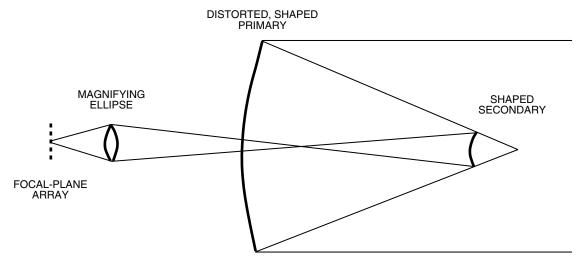
Fig. 2. Geometry for the focal-plane array physical optics calculation.

B. Qualitative Results

As was mentioned above, the first subject of investigation is the ability of the focal-plane array to compensate for the gravity distortion of the primary reflector as the antenna tips in elevation angle. The next three figures illustrate how this compensation occurs. The results presented here are intended to be qualitative only. Quantitative results follow in the next section.

Figure 3(a) shows the primary focal-plane distribution when the antenna is receiving at an elevation angle of 45 deg. In this particular case, the x- and y-axis scales are in pixel units rather than engineering units. For this particular elevation angle, the distortion is minimum, and a well-formed spot is visible. The energy distribution is well-matched to a corrugated feed horn and can be efficiently collected. If the energy is not collected but is allowed to pass through the re-imaging optics and onto the focal-plane array, we may compute the array element excitation, as shown in Fig. 3(b). For this particular magnification, the energy falls primarily on 9 pixels and is efficiently collected.

Figure 4 shows identical information when the antenna elevation angle is 15 deg. Now a distorted spot appears at the primary focal plane in Fig. 4(a). Clearly this distorted spot will not be collected with high efficiency by a circular horn. In addition, energy appears in secondary lobes in the focal plane. After passing through the re-imaging optics, the energy falls upon the focal-plane array and is efficiently collected there, as shown in Fig. 4(b).

Finally, the extreme case of an elevation angle of 85 deg is illustrated in Fig. 5. In this case, the antenna is severely distorted and the primary focal-plane distribution is multi-lobed in Fig. 5(a). Only a few percent of this energy is available for coupling into a standard corrugated feed horn. Next the energy passes through the re-imaging optics and onto the focal-plane array, where it can be collected with relatively high efficiency, as shown in Fig. 5(b). For the first time, the image flip that occurs between the primary and secondary focal planes is visible in this figure. Although this flip is present for all results, the near symmetry of the results makes it difficult to detect in the previous two figures.

These results illustrate the advantage of the focal-plane array relative to a single feed horn for this particular application. Even though the energy is significantly spread out in the focal plane, it can be collected efficiently by the array. Though not illustrated directly, a pointing error of the antenna can be handled as well. For example, if a pointing error occurs, the spots simply slide left/right, up/down in the focal plane. Considering the results of Fig. 3, one can see that a wide range of motion of the spot, and hence a large pointing error, can be accommodated before the spot falls off the array. The array performance in the presence of pointing error will be discussed quantitatively later.
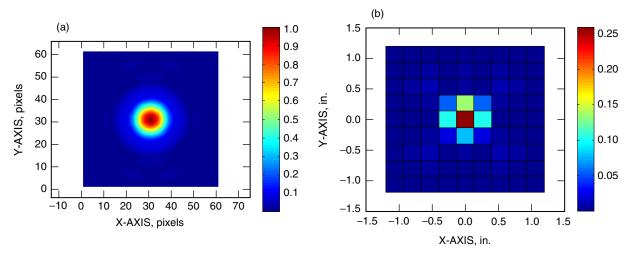
4

Fig. 3. An antenna receiving at a 45-deg elevation angle: (a) received focal-plane distribution and (b) array excitation.
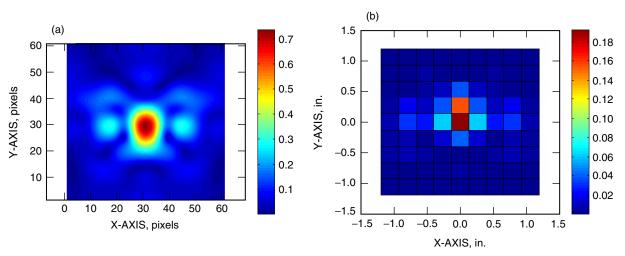

Fig. 4. An antenna receiving at a 15-deg elevation angle: (a) received focal-plane distribution and (b) array excitation.
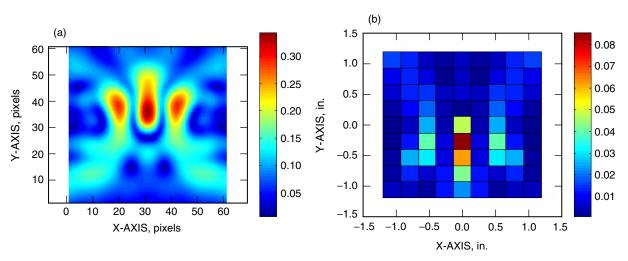

Fig. 5. An antenna receiving at an 85-deg elevation angle: (a) received focal-plane distribution and (b) array excitation.

5

C. Compensation of Gravity-Induced Surface Distortions

In this section, we address the quantitative performance of the array for gravity compensation as a function of the number of elements in the array and the magnification factor. Clearly, increasing the number of elements, or equivalently the size of the array, will always be beneficial, regardless of the magnification. This is true since larger arrays have access to more of the focal-plane energy, although the benefit can clearly be outweighed by the cost and complexity of the array, which grows in proportion to the number of elements.

The effect of magnification on performance, given a fixed array size, is more complex. For the definition of magnification used here, the spot size in the secondary focal plane is reduced as the magnification is increased. This allows more energy to be collected, offering an advantage for increased magnification. On the other hand, as the spot size is reduced, the size of a given patch relative to the feature size of the spot increases. This lack of resolution causes inefficiency in the coupling of the spot energy into the individual patch. Indeed, in the limit of extreme magnification, the entire spot, 100 percent of the focal plane energy, could be focused onto a single patch. The response of the patch would be poorly matched to the spot distribution, and a significant coupling loss would occur. Clearly there is trade-off involving the magnification, array size, and performance across all antenna elevation angles. This is the subject of the next few figures.

Figure 6 plots the computed antenna efficiency versus elevation angle and number of array elements for a re-imaging magnification factor of two. Here antenna efficiency is defined as the ratio of computed physical optics gain to the theoretical gain of a 70-m circular aperture with uniform illumination. For the undistorted dual-shaped antenna, this efficiency approaches 91 percent when a matched corrugated horn is used as the feed. In practice, many additional losses, such as high-order surface errors, panel setting, secondary positioning, etc., will reduce this 'theoretical' efficiency further. For the purposes of this study, these effects are ignored.
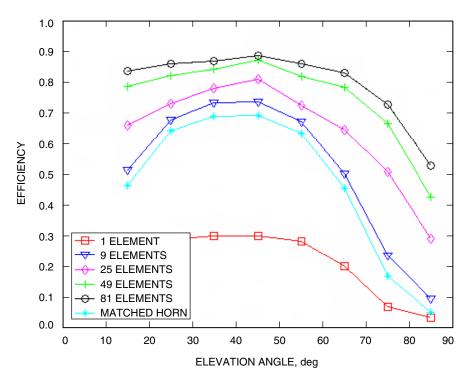

Fig. 6. Antenna efficiency versus elevation angle and array size for a magnification factor of 2.

In this case as well as those that follow, we plot results for efficiency versus elevation angle for arrays containing 1, 9, 25, 49, and 81 elements, as well as those for a matched corrugated horn as a comparison. The horn result is effectively the performance of the antenna as presently configured. For this particular set of distortions, we see that the horn feed, the cyan curve, achieves only 70 percent efficiency near an elevation angle of 45 deg, whereas over 90 percent is theoretically available. This is due to the residual distortion of the antenna present at 45 deg. This efficiency falls to below 50 percent for an elevation angle of 15 deg and below 5 percent for an extreme elevation angle of 85 deg. For this particular magnification, a 9-element array covers approximately the same area as the matched horn and gives similar performance. Larger arrays are increasingly more effective in capturing the focal-plane energy at an elevation angle removed from 45 deg. The 81-element array improves the efficiency at 85-deg elevation from less than 5 percent to greater than 50 percent. The array is also effective in recovering the efficiency lost due to the residual distortion at 45 deg. Apparently there is still significant energy spilling past the array for elevation angles larger than 70 deg. The situation can be improved by increasing the magnification of the re-imaging optics.

Figure 7 shows results for a magnification factor of three. In this case, the 81-element efficiency at an elevation angle of 85 deg is increased to more than 65 percent. For this magnification, even the 9-element array has significantly improved performance relative to the horn for large elevation angles.

Finally, results for a magnification factor of 4 are shown in Fig. 8. Performance for the 81-element array at 85 deg is improved to near 70 percent. From this point on, only marginal returns are realized by increasing the magnification further. As discussed above, this is a result of the increased size of the patch element relative to the feature size in the focal-plane spot.

Figure 9 illustrates this point by plotting efficiency versus elevation angle for an 81-element array for the three choices of magnification, 2, 3, and 4. All array results are superior to the single-horn result. Increasing magnification improves array performance for large elevation angles, but actually degrades
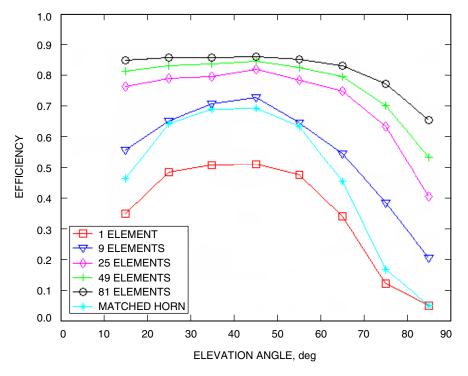

Fig. 7. Antenna efficiency versus elevation angle and array size for a magnification factor of 3.
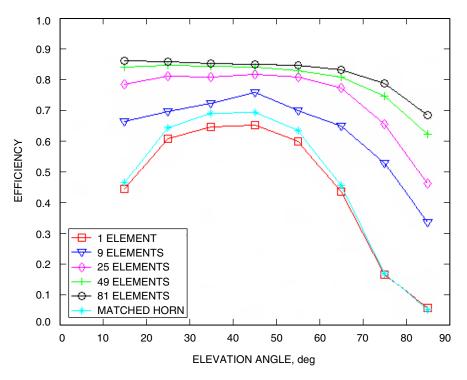
Fig. 8. Antenna efficiency versus elevation angle and array size for a magnification factor of 4.
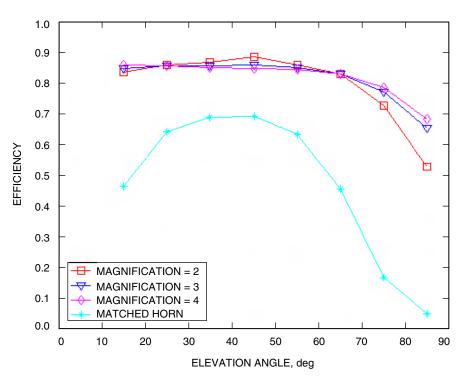

Fig. 9. Antenna efficiency versus elevation angle and magnification for an 81-element array.

performance near 45 deg. This is because the results for large elevation angles are dominated by the advantage of large magnification values putting more energy on the array, despite the loss in resolution of an individual element. On the other hand, near elevation angles of 45 deg, the spot extent is small and the results are dominated by the decrease in element resolution; hence, increasing the magnification actually hinders the performance of the array.

The above results illustrate the benefits of the focal-plane array over a single-horn feed for an antenna with severe elevation-dependent distortion, such as the DSN 70-m antenna. Although this antenna represents the greatest challenge for operation at 32 GHz in the DSN, the 34-m antennas can benefit from the array as well. For these antennas the elevation distortion is less severe, but other distortions occur as well, and these can also be compensated for by the array. For example, wind-induced and thermally induced distortions can be compensated for in exactly the same way as gravity-induced distortions, assuming that their time scale is consistent with the bandwidth of the signal-processing scheme used to combine the signals from the array. Another significant source of gain loss in DSN antennas operating at 32 GHz is secondary positioning error. This error is much more benign than 70-m gravity distortions and can also easily be compensated for by the focal-plane array.

D. Compensation of Antenna-Pointing Errors

Pointing error is also a significant source of gain loss for the large antennas of the DSN at 32 GHz. Presently a complex monopulse pointing system is used to aid in pointing the DSN 34-m antennas at 32 GHz. The blind-pointing requirement on the antennas is driven by the pull-in range of this monopulse system, requiring elaborate pointing models and calibration. Use of a focal-plane array eliminates the need for a monopulse system entirely and greatly reduces the requirements on blind-pointing accuracy and associated calibration effort.

Figure 10 shows the gain of the 70-m antenna for signals appearing off-boresight when a single corrugated horn is used as the feed, and for the case of an 81-element array used with a re-imaging magnification factor of three. The response for the single-horn feed effectively is that of a uniform aperture, resulting in a 3-dB beam width of approximately 7.5 mdeg. Therefore, in practice the antenna must be pointed, without feedback, to approximately this accuracy before an active pointing-control system, such as a monopulse system or conical scan, can be employed to actively point to the beam peak. The response of the focal-plane array to off-axis signals is quite forgiving, as illustrated by the black curve in the figure. In this case, the response is not limited by the inherent beam width of the antenna, but rather by the field of view of the array. For this particular magnification and array size, pointing errors of greater than ± 20 mdeg can be accommodated by the array with essentially no gain loss. These pointing requirements are consistent with typical 8-GHz (X-band) values, allowing operation of the 70-m antenna at 32 GHz with no requirement for an additional active pointing system or improvements to the present blind-pointing performance of the antenna. While illustrated here for the 70-m antenna, exactly the same advantages exist for application of the array on a smaller, 34-m DSN antenna. Relaxation of antenna-pointing requirements is considered a major advantage of the focal-plane array over a single-horn feed.

The next subsection describes the algorithms required to accomplish the optimum combination of the focal-plane array signals in the presence of both noise and interference, real effects that have been ignored in the performance estimates in Subsections III.C and III.D.

E. Optimum Weight Estimation by Means of the Least Mean-Square (LMS) Algorithm

The array output voltages are downconverted to complex baseband and sampled at a rate commensurate with the data bandwidth, that is, at the Nyquist rate. The vector of complex samples serves as the input to the signal-processing assembly, which estimates the optimum combining weights, performs multiplication of the signal samples by the optimum complex weights, and combines the weighted signals to provide a single output with maximum signal-to-noise ratio (SNR), or, in case there is spatially resolved interference, the maximum signal-to-interference-noise ratio (SINR).
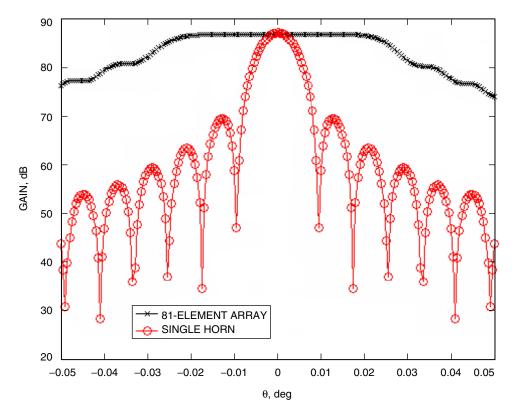
Fig. 10. Antenna gain versus pointing angle for the 81-element, magnification-3 array feed system and a single conventional corrugated feed horn.

The complex signal sample at time n in the ith channel can be represented as $s_i(n)$, and additive noise samples originating in the ith channel amplifier are denoted by $v_i(n)$. These noise samples are assumed to be independent from sample to sample in each channel, as well as between channels. In addition to amplifier noise, the focal-plane array may collect correlated noise samples originating from unresolved sources within the FPA's field-of view, such as from a planet. Extended planetary sources can be represented as clusters of point sources; however, here we consider only a single interfering point source, with downconverted samples $b_i(n)$. As shown in Fig. 11, the observed signal vector consists of three vector components, namely signal samples, amplifier noise samples, and point-source interference samples:

$$\mathbf{u}(n) = \mathbf{s}(n) + \mathbf{b}(n) + \mathbf{v}(n)$$

For a vector of complex array signals accompanied by additive noise, a set of optimum weights exists that maximizes the SINR of the combined sum. As derived in [9] by direct application of the Schwarz inequality specifically for the case of focal-plane array signals observed in the presence of statistically independent additive noise, the optimum weights are proportional to the conjugate of the signal divided by the variance of the additive noise. Therefore, the optimum weight in the ith channel is of the form $w_i(n) = s_i^*(n)/\sigma_i^2$, where σ_i^2 denotes the variance of the additive noise in the ith channel. For the case of correlated noise, generated by a combination of point-source interference and amplifier noise, the optimum weight vector that maximizes the SINR is known as the Wiener solution, and is of the form $\tilde{\mathbf{w}} = \mathbf{R}^{-1}\mathbf{p}$, where $\mathbf{R}$ is the covariance matrix of the observable vector,

$$\mathbf{R} \equiv E\,\mathbf{u}(n)\mathbf{u}^H(n) = E\,\mathbf{s}(n)\mathbf{s}^H(n) + E\,\mathbf{b}(n)\mathbf{b}^H(n) + E\,\mathbf{v}(n)\mathbf{v}^H(n) = [r_{ik}]$$
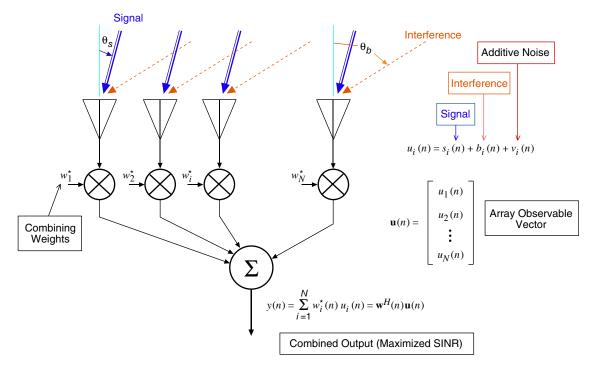
Fig. 11. Generalized adaptive combiner conceptual block diagram, identifying horn elements, signal source and interference direction, complex weights, and summer.

and where the correlation between the desired output signal samples $d(n)$ and the observable vector $\mathbf{u}(n)$ is defined as $\mathbf{p} = E\,\mathbf{u}(n)d^*(n)$. For the case of modulated signals, the desired signal may consist of known frame markers in the data stream, partially decoded data symbols obtained from hard decisions, or preliminary symbol estimates from the decoder itself.

Defining the error signal $e(n)$ as the difference between the desired output, $d(n)$, and the output of the array, $y(n) = \mathbf{w}^H(n)\mathbf{u}(n)$, the error signal can be expressed as $e(n) = d(n) - y(n) = d(n) - \mathbf{w}^H(n)\mathbf{u}(n)$. Next, define the cost function $J(\mathbf{w})$ as the mean-squared error, and let $J_{\min} = J(\tilde{\mathbf{w}})$, where the tilda indicates the optimum weight vector. Applying the definition of mean-squared error directly, it follows that [10]

$$J(\mathbf{w}) = E\,|e(n)|^2 = E\,|d(n)|^2 - \mathbf{w}^H\mathbf{p} - \mathbf{p}^H\mathbf{w} + \mathbf{w}^H\mathbf{R}\,\mathbf{w}$$

$$= E\,|d(n)|^2 - \mathbf{p}^H\mathbf{R}^{-1}\mathbf{p} + (\mathbf{w} - \mathbf{R}^{-1}\mathbf{p})^H\mathbf{R}\,(\mathbf{w} - \mathbf{R}^{-1}\mathbf{p})$$

$$= J_{\min} + (\mathbf{w} - \tilde{\mathbf{w}})^H\mathbf{R}\,(\mathbf{w} - \tilde{\mathbf{w}})$$

Given an arbitrary initial weight vector, $\mathbf{w}(0)$, a well-know approach to minimizing cost in optimization is the method of "steepest descent," which can be described as the following two-step procedure:

(1) Generate a sequence of weight vectors $\mathbf{w}(0), \mathbf{w}(1), \cdots, \mathbf{w}(n), \mathbf{w}(n+1), \cdots$ such that the average cost is reduced at each iteration: $J\big(\mathbf{w}(n+1)\big) < J\big(\mathbf{w}(n)\big)$.

(2) At each step, adjust the weight vector in the direction opposite to the gradient of the cost function, $\nabla J(\mathbf{w})$.

The steepest descent algorithm (SDA) is formally defined in vector form as

$$\mathbf{w}(n+1) = \mathbf{w}(n) - \frac{1}{2}\mu\,\nabla J\big(\mathbf{w}(n)\big)$$

Since $\nabla J\big(\mathbf{w}(n)\big) = 2\mathbf{R}\mathbf{w}(n) - 2\mathbf{p}$, the SDA can be rewritten as follows:

$$\mathbf{w}(n+1) = \mathbf{w}(n) - \mu\,[\mathbf{R}\,\mathbf{w}(n) - \mathbf{p}]$$

The parameter μ is called the step size; it controls both the rate of convergence and the steady-state SINR achieved by the combined output after convergence. If the theoretical expected values in the gradient are replaced by their instantaneous values, available at each update in a real implementation, we arrive at the LMS algorithm. Substituting instantaneous estimates for the expected values in the update equation, and carrying out the implied operations, yields

$$\mathbf{w}(n+1) = \mathbf{w}(n) - \mu\,[\mathbf{R}\,\mathbf{w}(n) - \mathbf{p}] \cong \mathbf{w}(n) - \mu\,\big[\mathbf{u}(n)\,\mathbf{u}^H(n)\,\hat{\mathbf{w}}(n) - \mathbf{u}(n)d^*(n)\big]$$

$$= \mathbf{w}(n) - \mu\,\mathbf{u}(n)\,\big[\mathbf{u}^H(n)\,\hat{\mathbf{w}}(n) - d^*(n)\big] = \mathbf{w}(n) - \mu\,\mathbf{u}(n)\,\big[\hat{\mathbf{w}}^H(n)\mathbf{u}(n) - d(n)\big]^*$$

$$= \mathbf{w}(n) - \mu\,\mathbf{u}(n)\big[\,y^*(n) - d^*(n)\big] = \mathbf{w}(n) - \mu\big[\,y^*(n) - d^*(n)\big]\mathbf{u}(n)$$

The right-hand side (RHS) of the last equality represents the conventional form of the LMS update algorithm. Note that the expected value of the LMS descent vector is of the form

$$E\,\mathbf{u}(n)\big[\,y^*(n) - d^*(n)\big] = E\,\mathbf{u}(n)\,\big[\mathbf{u}^H(n)\,\mathbf{w}(n) - d^*(n)\big]$$

$$= E\,\big[\mathbf{u}(n)\,\mathbf{u}^H(n)\,\mathbf{w}(n) - \mathbf{u}(n)d^*(n)\big] = \mathbf{R}\,\mathbf{w}(n) - \mathbf{p}$$

This demonstrates that the expected value of the LMS descent vector approaches zero as $\mathbf{R}\mathbf{w}(n) = \mathbf{p}$, or equivalently when $\mathbf{w}(n) = \mathbf{R}^{-1}\mathbf{p} \equiv \tilde{\mathbf{w}}(n)$, and hence stops updating the weights when the optimum weight vector is achieved. This is the solution that maximizes the SINR of the combined output [10]. When there is no interference, the optimum weight vector is proportional to the signal vector itself: $\tilde{\mathbf{w}} \propto \mathbf{s}$. When interfering sources are present, the optimum solution maximizes the combined SINR, effectively minimizing the interference by means of spatial filtering while transmitting the required signal power to achieve optimum performance.

1. LMS Algorithm Simulation Results. Performance of the LMS algorithm has been evaluated by means of simulations. The FPA excitations were computed with the assumption of an undistorted antenna, for both an unmodulated signal source at normal incidence and an interfering, unresolved thermal point source offset from the signal by approximately an antenna beam width.

First, consider the effect of step size on LMS convergence. Two cases of the time history of the combined output, when the LMS starts with the all-zeros weight vector, are shown in Figs. 12(a) and 12(b). Note in Fig. 12(a) that with a step size of 0.0007, meaning that only this fraction of the current update is applied to the weight vector, convergence takes place in approximately 1000 samples (this is where the combined output reaches its steady-state value). When the step size is increased by a factor of 10, the output converges to its final value in approximately 100 samples, or one-tenth the time, but also becomes
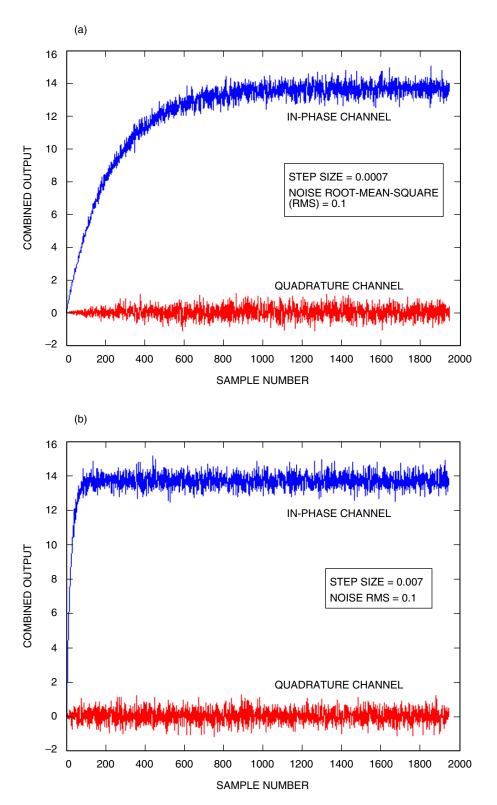
Fig. 12. LMS adaptive combining algorithm performance in noise with (a) small step size and (b) large step size.

somewhat noisier due to less accurate combining-weight estimates. Although in Figs. 12(a) and 12(b) the observed performance degradation is minimal, it can become prohibitive with large step size, implying that a "best" value exists even for steady-state problems (that is, problems where the optimum weights do not change with time). When channel dynamics are significant, the minimum step size is generally determined by the convergence rate required to track the signal (hence weight) dynamics; in this case, there is generally an optimum step size, one that best balances the conflicting requirements of rapid response and noise reduction through longer effective integration.

When the signal is observed in the presence of an interfering point source (such as an unresolved planet) as well as additive noise, the behavior of the LMS algorithm becomes more complex. Typical behavior is illustrated in Fig. 13, which clearly indicates an "interference cancellation" region, in addition to the monotonic convergence to a steady-state value considered previously. When the interference power is much greater than the power of the additive noise, it tends to dominate the SINR until its direction of arrival is adequately determined by the LMS algorithm and an effective null of the array pattern is steered in the direction of the interference. The degree to which this can be accomplished depends on the number of degrees of freedom in the FPA (roughly the number of array elements) and the separation of the interference from the signal source: if the interference is much closer to the signal source than the angular resolution of the antenna, little improvement is possible because nulling the interference also results in nulling of the signal source. However, when the source-interference separation is a significant fraction of a beam width or greater, then distorting the beam can result in greater interference suppression with minimal signal attenuation, resulting in improved SINR. In general, the stronger the interference, the faster the algorithm estimates its direction, and the faster it can adjust the combining weights in order to suppress it. The example of Fig. 13 shows that even with a relatively large step size of 0.001, convergence to steady-state SINR occurs after about 3000 samples, which is about 3 times longer than required with additive noise alone (at a comparable step size of 0.0007). This additional time to convergence must be taken into account when attempting to adaptively cancel an interference with time-varying relative geometry, such as would occur with a spacecraft orbiting a distant planet.
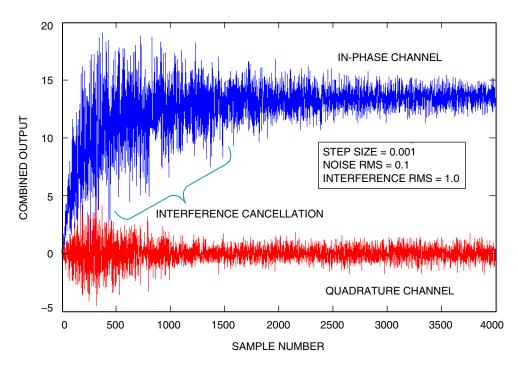

Fig. 13. LMS algorithm convergence in the presence of strong nearby interference.

IV. Focal-Plane Hardware Architecture

In this section, we discuss some details regarding the focal-plane array hardware. A typical microwave focal-plane array using patch antennas would require that the electrical length from the focal plane to the combing junction be equal to a small fraction of a wavelength. The signal-combing process used in this system does not have that requirement. The phase difference between elements can be arbitrary within reason. The freedom in differential path length substantially simplifies the design requirement for the antenna.

The optimum array element spacing for this application is to have a minimum gap size between elements. Given this spacing requirement, it is difficult to configure the 9×9 array under consideration on a single board. There is no room between elements for the transmission lines from the patches to the LNAs. Connecting the patches in tandem behind the focal plane was considered but was deemed impractical. Coaxial connections would be mechanically difficult to implement. The mechanical tolerancing of pin vias was also considered too demanding.

The construction considered here is a stacked construction using offset square layers. A schematic of the conceptual design is shown in Fig. 14. A similar technique using offset layers of elements has been used successfully for a 7×8 focal plane array at 32 GHz for a radio astronomy application [6]. The square, stacked approach allows easy access to all the elements, allows room for connection of the LNAs, and leaves room for bias lines. The patches shown are typical for a linearly polarized receiver. A detailed design of the required patches for circularly polarized signals would be needed for implementation.

V. Cryogenic System Design

One of the key challenges of designing a cryogenically cooled array system is developing a design that is capable of maintaining the array elements at the desired temperature and providing interfaces for the input and output RF signals and the power supply interfaces for the LNAs. The key cryogenic design issues include cooling the array patch elements and LNAs while providing adequate thermal isolation, providing a suitable microwave window to allow the input signal to enter the cooled space, and providing a practical method for routing the output transmission lines and LNA bias into the cooled space.

A. Cryogenic Cooling

The basic design of the cryocooler is similar to existing DSN LNA coolers. The cryogenic cooling is supplied by a commercial 4-K Gifford–McMahon (GM) cooler with 1.5 W of cooling at 4 K. An additional cooling stage provides 30 W of cooling at 50 K for intercepting radiation and conductive loads.
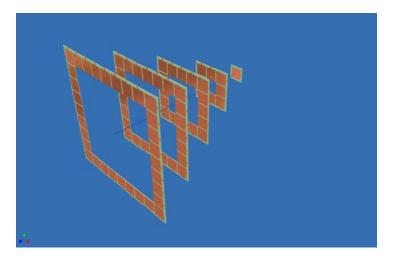

Fig. 14. Stacked-layer patch array concept.

15

The cooler is enclosed in a cylindrical 25-cm-diameter vacuum housing to provide insulation. A cylindrical thermal radiation shield is attached to the 50-K stage of the cooler and surrounds all of the 4-K components. The radiation shield has a circular opening for the feed energy entering from the window and has openings radially for the output transmission lines on the side of the cylinder. The antenna elements and LNA elements are attached with a heat sink to the 4-K stage of the cooler with conductive epoxy. A conceptual layout of the system is shown in Fig. 15.

B. Thermal Design

Thermal radiation from room temperature to the patch array is the largest cryogenic heat load. A 4-cm-square array with an estimated emissivity of 0.6 would require 0.47 W of cooling. This is acceptable but can be reduced by using a series of floating radiation shields using polystyrene blocks. Five blocks 1-cm thick would reduce the heat load by a factor of 9 to 0.05 W [7]. The measured noise temperature of polystyrene is 0.1 K per centimeter of thickness [8] and would contribute 0.5 K. In addition to reducing the cryogenic heat load, the radiation shielding reduces the radiation cooling of the input window and eliminates any condensation on the window from moisture in the air outside the window.

C. Cryogenic Transmission Line Design

The construction of the patch array/LNA considered here lends itself to a very simple cryogenic feed-through interface for the RF output and LNA bias lines. The micro-strip antenna patches are connected to strip-line transmission lines consisting of thin (<1 mm) low thermal conductivity substrates with very thin (<0.1 mm) metallic conductors. The circular stacked array element boards are bonded to insulator rings at the circular vacuum cylinder walls and sandwiched between the cylinder walls with conventional O-ring seals. The connections for amplifier bias are thin metallic conductors sandwiched with the RF transmission lines. The resulting thermal resistance from the cooled antenna/LNA assembly to ambient temperature will be high, resulting in a low cryogenic heat load.
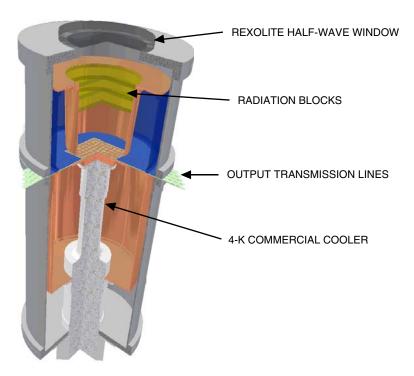

Fig. 15. Conceptual layout of the cooled FPA.

D. Microwave Input Window

The input window design chosen is a 1/2-wave (6.4-mm) Rexolite plate. Rexolite is a polystyrene solid and has been used for a number of 32-GHz feed window applications in DSN research and development systems. The measured noise contribution of this window is 1.6 K [8].

E. System Noise Temperature

Due to the fact that the entire feed and LNA on this system will be cooled to 4 K, the system noise temperature of the antenna–LNA combination should rival the performance of existing DSN systems. The contributors to the noise temperature are the microwave input window, the antenna/transmission line, the LNA MMIC, and the receiver follow-on temperature. A patch antenna and strip-line transmission line would normally not be considered in a low-noise application. Because this system is cooled to 4 K, the noise contribution from the transmission line is small. A transmission line with a 1-dB loss at 300 K would contribute 62 K. If the loss is cooled, the contribution decreases in ratio to the absolute temperature. A 1-dB loss at 4 K contributes 0.8 K. Table 1 shows the expected noise budget of the system. The noise performance is dominated by the LNA contribution.

Table 1. System noise temperature estimate.

Contributor	Contribution, K	Notes
Window	1.6	Measured data
Radiation blocks	0.5	Measured data
Antenna/transmission line	0.8	Assume 1-dB loss at 4 K
LNA MMIC	15	Estimate
Receiver follow-on	0.3	3-dB noise figure, 30-dB LNA gain
Total system noise temperature	18.2	—

VI. Summary and Conclusions

The operational advantages of a focal-plane array receiver for use on the large antennas of the Deep Space Network have been discussed. The example of gravity compensation of the 70-m antenna gravity distortions during 32-GHz operation has been chosen to illustrate these operational advantages. In addition, an algorithm for the optimum combining of the array signals in a noisy environment including interference was described. Strawman mechanical and cryogenic designs were also presented, along with a noise temperature estimate for the system.

References

[1] V. Vilnrotter and D. Fort, "Demonstration and Evaluation of the Ka-Band Array Feed Compensation System on the 70-Meter Antenna at DSS 14," *The Telecommunications and Mission Operations Progress Report 42-139, July–September 1999*, Jet Propulsion Laboratory, Pasadena, California, pp. 1–17, November 15, 1999. http://ipnpr/progress_report/42-139/139J.pdf

[2] V. B. Khaikin, E. K. Majorova, Yu. N. Parijskij, M. D. Parnes, R. G. Shifman, V. A. Dobrov, V. A. Volkov, V. D. Korolkov, and S. D. Uman, "7 × 8 Element MMIC Array at 26-30 GHz for Radio Astronomy Applications," *Proceedings of International Conference: "Perspective on Radio Astronomy: Technologies for Large Antenna Arrays*, Dwingeloo, The Netherlands, pp. 171–182, April 12–14, 1999.

[3] P. W. Cramer, "Initial Studies of Array Feeds for the 70-Meter Antenna at 32 GHz," *The Telecommunications and Data Acquisition Progress Report 42-104, October–December 1990*, Jet Propulsion Laboratory, Pasadena, California, pp. 50–67, February 15, 1991.
http://ipnpr/progress_report/42-104/104E.PDF

[4] W. A. Imbriale, M. J. Britcliffe, and M. Brenner, "Gravity Deformation Measurements of NASA's Deep Space Network 70-Meter Reflector Antennas," *The Inter-Planetary Network Progress Report 42-147, July–September 2001*, Jet Propulsion Laboratory, Pasadena, California, pp. 1–15, November 15, 2001.
http://ipnpr/progress_report/42-147/147I.pdf

[5] W. L. Stutzman and G. A. Thiele, *Antenna Theory and Design*, second edition, New York: John Wiley and Sons, Inc., pp. 210–218, 1998.

[6] V. Khaikin, V. Dobrov, M. Parnes, V. Volkov, A. Golovkov, and Yu. Rybakov, "Multi-Channel Array Receiver Modules for a Radio Telescope at 26-30 GHz," *Proceedings of URSI/IEEE XXVII Convention on Radio Science*, Espoo, Finland, pp. 176–178, October 2002.

[7] R. F. Barron, *Cryogenic Systems*, New York: Oxford University Press, pp. 386–387, 1985.

[8] M. J. Britcliffe, T. R. Hanson, and M. M. Franco, "Cryogenic Design of the Deep Space Network Large Array Low-Noise Amplifier System," *The Interplanetary Network Progress Report*, vol. 42-157, Jet Propulsion Laboratory, Pasadena, California, pp. 1–13, May 15, 2004. http://ipnpr/progress_report/42-157/157C.pdf

[9] V. A. Vilnrotter, E. R. Rodemich, and S. J. Dolinar, "Real-Time Combining of Residual Carrier Array Signals Using ML Weight Estimates," *IEEE Transactions on Communications*, vol. 40, issue 3, pp. 604–615, March 1992.

[10] S. Haykin, *Adaptive Filter Theory*, fourth edition, New Jersey: Prentice Hall, 2002.